nature geoscience

ARTICLES

https://doi.org/10.1038/s41561-019-0347-1

Seismic velocity reduction and accelerated recovery due to earthquakes on the Longmenshan fault

Shunping Pei[1,2], Fenglin Niu[3,4]*, Yehuda Ben-Zion[5], Quan Sun[2], Yanbing Liu[2], Xiaotian Xue[2], Jinrong Su[6] and Zhigang Shao[7]

Various studies report on temporal changes of seismic velocities in the crust and attempt to relate the observations to changes of stress and material properties around faults. Although there are growing numbers of observations on coseismic velocity reductions, generally there is a lack of detailed observations of the healing phases. Here we report on a pronounced coseismic reduction of velocities around two locked sections (asperities) of the Longmenshan fault with a large slip during the 2008 M_w 7.9 Wenchuan earthquake and subsequent healing of the velocities. The healing phase accelerated significantly at the southern asperity right after the nearby 2013 M_w 6.6 Lushan earthquake. The results were obtained by joint inversions of travel time data at four different periods across the Wenchuan and Lushan earthquakes. The rapid acceleration of healing in response to the Lushan earthquake provides unique evidence for the high sensitivity of seismic velocities to stress changes. We suggest that stress redistribution plays an important role in rebuilding fault strength.

Earthquakes are caused by the rapid conversion of stresses to inelastic strain (rock damage) along faults[1–10]. Recent studies show that fault failure can manifest as a small or large earthquake[11], as a seismic slip[12] or as non-volcanic tremor[13–15]. It is also found that fault interactions and other processes can significantly affect the long-term stress build up by plate tectonics[16,17]. In principle, stress transfer can be calculated with elastic or viscoelastic modelling[16–21]; however, to estimate the stress changes from data is notoriously difficult, particularly at seismogenic depths. One promising approach is to accurately monitor changes of subsurface seismic velocities[4,22], which are shown in laboratory studies to be sensitive to the stress field[23–25] due to stress-induced changes in the properties of cracks. Indeed, an increasing number of observations on temporal changes of seismic velocities are associated with the occurrence of tectonic events, such as earthquakes[3–8,26–28] and volcanic eruptions[29,30].

The Longmenshan fault zone is located at a pronounced topographic boundary between the eastern margin of the Tibetan plateau and the western Sichuan basin (Fig. 1), where the elevation changes from ~5,000 m to ~500 m within a distance of ~50 km. Geologically, the fault zone manifests itself as the thrust front of the Himalayan orogen and consists of a series of low-angle transpressional faults that extend from southwest to northeast for approximately 300 km. Fault motion is dominated by thrust at the southwestern section and gradually transitions to strike slip at the northeastern end. Over the past decade, two major earthquakes, the 2008 M_w 7.9 Wenchuan earthquake (WCEQ) and the 2013 M_w 6.6 Lushan earthquake (LSEQ), ruptured the northeastern part and the southern end of the fault zone, respectively. The section between with a length of ~60 km remained intact and is associated with a seismic risk yet to be determined. The area was well instrumented before and after the earthquakes, which provides unique opportunities to study the temporal variations of seismic properties and the interaction among different segments of the fault zone.

The Longmenshan fault zone is in a seismically active region, which is closely monitored by the regional seismic network operated by the Earthquake Administration of Sichuan Province (EASP). The seismicity before the 2008 M_w 7.9 earthquake was rather diffuse and spread widely across the entire margin (black crosses in Fig. 1b). It was replaced by a much more condensed aftershock seismicity along the Longmenshan fault after the main shock (circles in Fig. 1b). These small events are well recorded and located by the EASP seismic network due to the good station coverage in both azimuth and distance.

Coseismic velocity reduction in the 2008 WCEQ

We selected the first P wave arrivals in the distance range between 0.1° and 2.0°, which are known as the Pg waves that travel through the upper crust, recorded in the period of 2000–2014. The Pg travel times exhibit a linear relationship with an epicentral distance (Supplementary Fig. 1) and the slope of the linear trend corresponds to the average velocity of the upper crust sampled by the source–receiver ray paths. We noticed a small yet systematic change in the slope of the travel time curve. We organized the travel time data in a chronological order, and divided the 15-year period into time intervals that contained roughly the same amount of earthquakes. In particular, we used one-year and one-month intervals before and after, respectively, the WCEQ due to the large number of

[1]CAS Center for Excellence in Tibetan Plateau Earth Sciences, Chinese Academy of Sciences (CAS), Beijing, China. [2]CAS Key Laboratory of Continental Collision and Plateau Uplift, Institute of Tibetan Plateau Research, Chinese Academy of Sciences (CAS), Beijing, China. [3]State Key Laboratory of Petroleum Resources and Prospecting, and Unconventional Gas Institute, China University of Petroleum at Beijing, Beijing, China. [4]Department of Earth, Environmental and Planetary Sciences, Rice University, Houston, TX, USA. [5]Department of Earth Sciences, University of Southern California, Los Angeles, CA, USA. [6]Earthquake Administration of Sichuan Province, Chengdu, China. [7]Institute of Earthquake Science, China Earthquake Administration, Beijing, China. *e-mail: niu@rice.edu

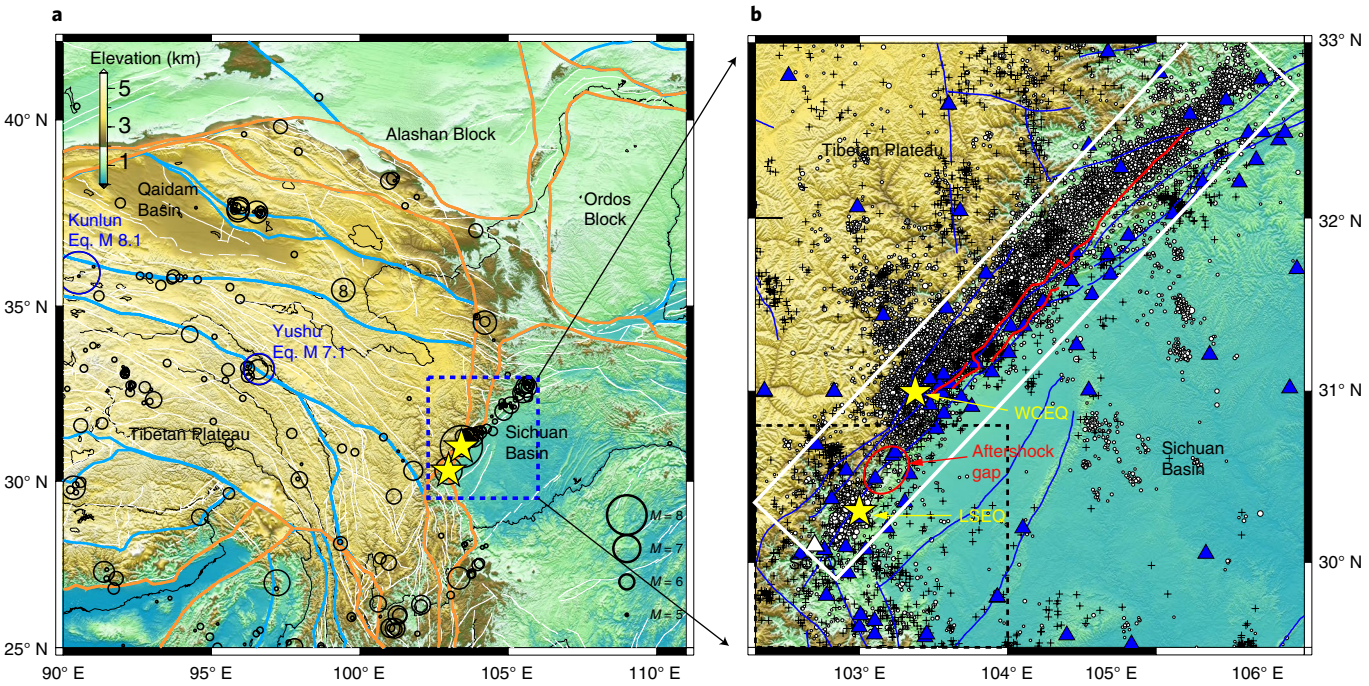

Fig. 1 | The topographic map shows the tectonic blocks around the 2008 M_w 7.9 WCEQ and 2013 M_w 7.0 LSEQ. a, The coloured thick lines and white thin lines indicate block boundaries and active faults, respectively. **b**, The solid blue triangles, the crosses and the circles represent seismic stations and earthquakes that occurred before and after the WCEQ, respectively. The blue lines indicate active faults and the red lines show the surface traces of the WCEQ. The dashed blue (**a**) and black (**b**) boxes indicate the two areas used to compute the average velocity changes shown in Fig. 2b. The white solid box outlines the Longmenshan fault zone. Eq, earthquake; M, surface-wave magnitude.

aftershocks. Using linear regressions of the Pg travel times compiled in each period, we computed the corresponding average P-wave velocities and observed a significant variation across the 15-year period (Fig. 2a). The estimated average P-wave velocity remained more or less the same, at ~6 km s^{-1} before the WCEQ, and dropped abruptly by nearly 4% to ~5.75 km s^{-1} right after the mainshock. It then rose gradually to ~5.85 km s^{-1} before the 2013 M_w 6.6 LSEQ, in which a small coseismic drop was observed. The influence from the LSEQ, however, appears to have had a very short duration and the recovery of P-wave velocity seems to be present one month after the LSEQ and continues to grow nearly to the level prior to the WCEQ.

To further locate the lateral distribution of the observed average velocity changes, we developed a tomography technique that jointly inverts the travel times observed at different time periods for two-dimensional (2D) subsurface velocity changes. We analysed four time periods that sampled just before and just after the two earthquakes, which are marked by black solid horizontal lines in Fig. 2a. The length of each period was chosen such that the four time periods have roughly the same amount of Pg travel time data. The large numbers of aftershocks immediately after the WCEQ means that a very short time period P2 is sufficient to accumulate the required amount of data, which produces a ~3-year gap between P2 and P3. We treated the Pg travel times in each period as independent observations and employed a 2D travel time tomography method[31,32] to jointly invert the data from the two consecutive periods for the background velocities of each lateral block as well as their changes between the two periods (Methods).

The coseismic velocity changes of the WCEQ (Fig. 3a) were obtained from the joint inversion of the Pg data for the first two time periods, P1 and P2. Large velocity drops were clustered at the Yingxiu Town of Wenchuan County and in Beichuan County, which are hereafter referred to as the Wenchuan asperity (WCA) and the Beichuan asperity (BCA). Note that these are spatially coincident with the two areas of large coseismic slip[33–35] and surface deformation[36,37]. Results from the joint inversion of the Pg data for the two time periods, P2 and P3, reveal post-seismic velocity changes that occurred in the four-year period following the mainshock and right before the 2013 LSEQ (Fig. 3b). During this period, most of the velocity recoveries occurred around the BCA, which suggests that fault healing during this period took place at this part of the fault. The WCA, however, showed very little to no velocity change during this period.

Accelerated healing following the 2013 LSEQ

The coseismic velocity changes of the LSEQ inverted from P3 and P4 (Fig. 3c) show a large velocity increase in the southern portion of the Wenchuan rupture zone, particularly in the area near the WCA. Velocity changes in other regions, which include the BCA area, are insignificant. We further computed the total amount of velocity recovery along the Longmenshan fault over the six-year period after the WCEQ by jointly inverting the P2 and P4 data (Fig. 3d). Most of the coseismic velocity drops of the WCEQ that were centred at the two asperity zones appear to nearly recover during this period.

To examine how seismic velocity has evolved in the two asperity regions, we computed the average velocities and their s.d. using cells in the black boxes marked in Fig. 3. The results are shown in Fig. 2b and can be summarized as follows. The WCEQ caused a coseismic velocity drop of ~0.2 km s^{-1} in both asperity zones. Then the two asperities had very different paths in their recovery process. The BCA has been recovering continuously, and does not seem to be affected by the occurrence of the LSEQ. The WCA, however, had a slow recovery at the beginning, followed by a rapid healing probably triggered by the LSEQ.

A chequerboard resolution test indicates that the spatial and temporal variations in the velocity structure along the Longmenshan fault zone can be resolved well by the Pg data (Supplementary Figs. 2–6).

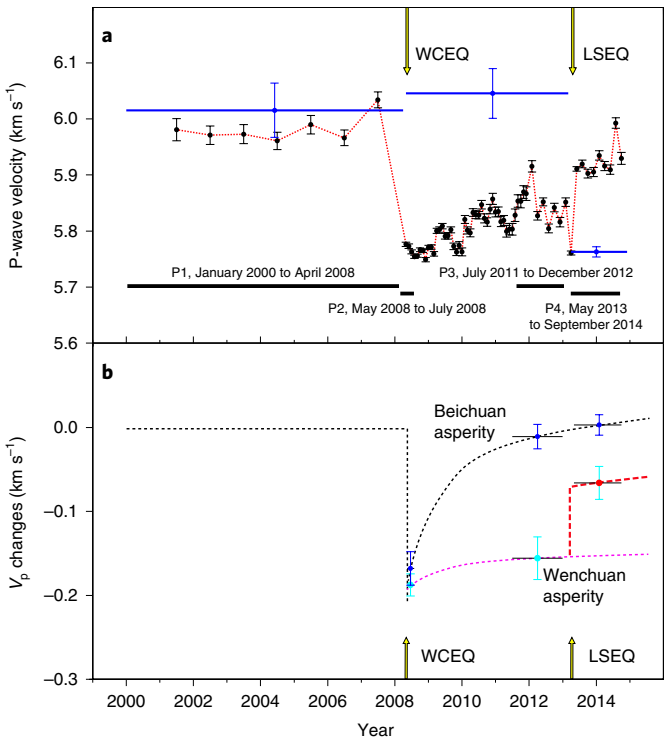

Fig. 2 | Temporal variations of crustal velocity structure beneath the Longmenshan fault zone. a, The averaged velocities calculated in the Longmenshan and Lushan areas are shown as black and blue dots, respectively. Error bars represent the corresponding s.d. The four black line segments (P1 to P4) show four time periods, for which the Pg travel times are used to image the temporal–spatial velocity changes. **b**, Observed velocity changes (V_p) of the WCA (cyan) and BCA (blue) shown together with the healing models. The velocities were computed by taking the averages of the square areas shown in Fig. 3.

Bootstrap analysis[38] also suggests that the observed temporal velocity changes are not produced by differences in earthquake location, source depth and station distribution (Supplementary Figs. 7 and 8). The observed coseismic velocity changes along the Longmenshan fault are consistent with previous estimates derived from ambient noise data[8–10]. This supports the interpretation that the temporal velocity changes revealed by the Pg data reflect the evolution of the Longmenshan fault zone during the major earthquake failures and the initial phase of the following healing and stress build up.

Coseismic velocity changes associated with large earthquakes have been observed widely, especially after the emergence of ambient noise imaging techniques. However, the depth that primarily affects the observed seismic velocity changes is less clear. In general, velocity changes can reflect the rock damage caused by a strong ground motion (which is expected to occur primarily in the top few hundreds of metres), structural changes within the rupture zone at depth, opening of cracks induced by changes of the stress field that can occur at various depth sections and related changes in the fluid content at different depth sections. Seismic velocity drops associated with shallow rock damage are observed with amplitudes of a few percent to tens of percent[1–7], whereas stress induced velocity changes are expected to be around a fraction of a percent. Several seismic studies found temporal velocity changes of ~0.4% after the WCEQ using ambient noise data[8,9]. As these analyses involved 10–25 s Rayleigh waves, the results were interpreted to reflect deformation that extends to seismogenic depth. A recent numerical study[39], however, shows that large changes in the shallow crust can affect Rayleigh wave phase velocities up to 20 s. Therefore, it is unclear whether the ~0.4% coseismic velocity drop observed by ambient noise studies truly reflects the stress-induced velocity changes at seismogenic depth.

Shaking from nearby or even distant great earthquakes can cause shallow fault damage when the fault has been weakened by a large local earthquake. Fault healing was observed to occur continuously after the 1992 Landers earthquake, but was temporally interrupted when the nearby M_w 7.1 Hector Mine occurred in 1999[40]. Strength recovery of the 2004 Parkfield earthquake fault also seems to be weakened by the distant M_w 9.1 Sumatra earthquake that occurred three months later[41]. Our observations of changes along the Longmenshan fault zone, however, reveal a completely opposite scenario. Fault healing can be accelerated by a nearby earthquake, which is difficult to explain by shaking-induced damage on weakened faults.

As most of the earthquakes used in this study occurred between 5 and 20 km, we expect that the observed temporal velocity changes at the asperity zones are not entirely caused by rock damage within the top a few hundreds of metres. To confirm this, we conducted inversions using only data from the stations located ~50 km away from the two asperities, and found that significant amounts of temporal changes are still imaged at the two asperities (Supplementary Fig. 8). We also conducted a 3D tomographic inversion with the same data and found consistently significant changes in the depth range 2–20 km (Supplementary Fig. 9). The weighted average velocity changes in the 3D tomography are very similar to those derived by the 2D inversion. This implies that a 2D inversion, which has fewer parameters, is suitable to image velocity changes with the types of data and geometry of the study area.

Stress-induced fault strengthening

The coseismic velocity drop observed at the WCA and BCA could be caused by both strong shaking and stress changes. In particular, stress is expected to play a major role in the observed accelerated healing that occurred at the WCA after the LSEQ (Fig. 2b). We computed the Coulomb stress transfer at the WCEQ rupture zone caused by the LSEQ and found that changes in both the normal and shear stress were nearly negligible (less than 1 Pa). Therefore, the observed velocity increase at the WCA is unlikely to be caused by the coseismic elastic stress transfer due to the slip on the LSEQ fault. It is also implausible that the velocity increase was induced by dynamic stress changes associated with passing seismic waves of the LSEQ, which can be larger than the static Coulomb stress transfer[42], but are expected to have transient rather than residual effects on the medium.

We speculate that the required larger stress change may be produced by the adjustment of stress loading between the plateau and the basin along their boundary, the Longmenshan fault, due to the occurrence of the LSEQ. In general, earthquake faults are highly heterogeneous and tend to be supported primarily by a few major locked asperities surrounded by partially creeping regions. The failure of the Lushan asperity (LSA) probably produced additional aseismic deformation that increased the load carried by the nearby WCA. In other words, the observed sudden velocity increase at the WCA was probably caused by the combined seismic and aseismic afterslip that followed the Lushan rupture zone. Such changes of deformation should be observable if near-field GPS data across the Longmenshan fault near the LSA and WCA were available. Interestingly, in situ stress measurements at a borehole (solid red circle in Fig. 3c) located ~35 km north of the LSEQ epicentre suggest that the minimum horizontal stress at ~160 m depth increased from ~5 MPa to ~12 MPa, whereas the maximum horizontal stress grew from ~5 MPa to ~22 MPa (ref. [43]). This gives an increase of stress by ~7–17 MPa. If we assume that the stress change at the WCA is of the same order, and use the observed P-wave velocity change at the WCA of about 1.7%, the calculated velocity-stress sensitivity ($\mathrm{d}\ln V/\mathrm{d}P$)

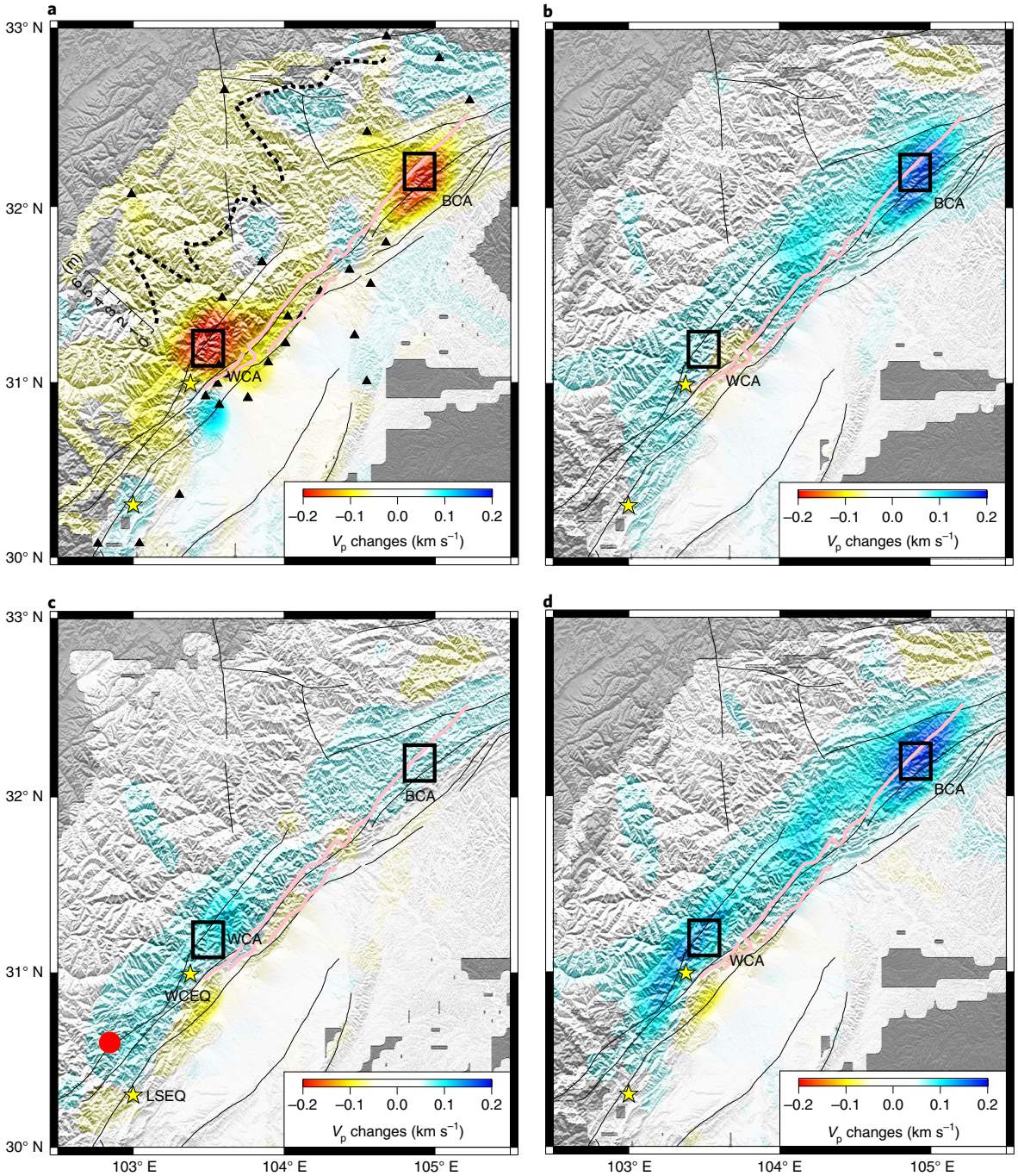

Fig. 3 | Spatiotemporal evolution of the velocity structure along the Longmenshan fault zone. a, Coseismic velocity decrease (red) and increase (blue) of the Wenchuan Earthquake (P2 – P1). The dashed line indicates the surface displacements along the faults (grey lines). **b**, Spatial variations of the post-seismic velocity recovery before the LSEQ (P3 – P2). **c**, Coseismic velocity changes of the LSEQ (P4 – P3). The solid red circle indicates the Qiaoqi borehole stress meter[42]. **d**, Spatial variations of the post-seismic velocity recovery after the LSEQ (P4 – P2). Pink lines represent the surface traces of the WCEQ.

is around $1.01–2.45 \times 10^{-9}$ Pa^{-1}. Laboratory measurements[23–25] and field observations[2,22] indicate that the stress sensitivity of the P-wave velocity at low confining pressures equivalent to shallow depths is in the range $10^{-10}–10^{-6}$ Pa^{-1} depending on the crack density in the rocks. It is therefore plausible that the observed velocity increase at the WCA after the LSEQ was produced by stress change that probably involves aseismic afterslip around the LSA.

The observed seismic velocity changes between different periods reveal the evolving coupling between the Tibetan plateau and the Sichuan basin along the Longmenshan fault zone during the past ten years (Fig. 4). Before the WCEQ and during period P1, the two blocks were locked and the stress was probably supported by the BCA, WCA and LSA (Fig. 4a). In the next period, P2, when the WCEQ occurred, a large portion of the Longmenshan fault in the north failed, which led to a coseismic velocity decrease across all the ruptured section, with two peaks collocated with two areas that have large coseismic slips, the WCA and BCA (Fig. 4b). The seismic velocity drop probably resulted from a combination of increasing rock damage in the fault zone and the reduction of normal stress. The WCEQ also caused a stress increase in the LSA, which shows

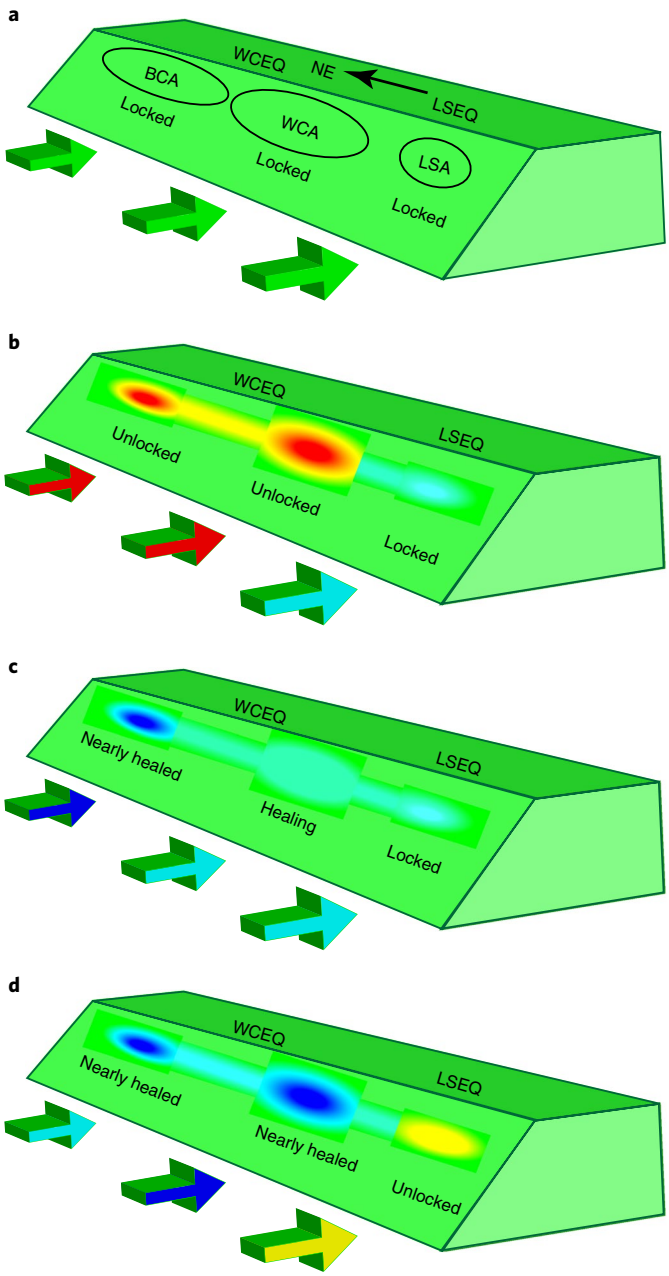

Fig. 4 | Evolution diagram of the Longmenshan fault zone in four different stages. a, P1, before the WCEQ. The BCA, WCA and LSA were locked before the two earthquakes. **b**, P2, after the WCEQ. The BCA and WCA were broken by the WCEQ and showed significant coseismic velocity drops. The earthquake also caused a slight velocity increase inside the LSA region. **c**, P3, before the LSEQ. About 5 years after the WCEQ, the BCA had mostly healed, but the WCA was still healing. **d**, P4, after the LSEQ. The LSEQ unlocked the LSA, which caused a coseismic velocity drop in the asperity area and a rapid acceleration in the healing at the WCA. NE, north east.

a small velocity increase in Figs. 2a (blue lines) and 3a. In the post-Wenchuan earthquake period P3, the velocity increase around the BCA took place much faster than at the WCA and almost reached the pre-earthquake level before the occurrence of the LSEQ (Fig. 4c). In the period P4, shortly after the LSEQ, the velocity recovery around WCA increased rapidly and nearly reached ~75% the pre-earthquake level approximately one year after the LSEQ. At the same time, a coseismic velocity drop occurred around the LSA (blue line in Fig. 2b), which suggests that the southwestern end of the Longmenshan fault is now unlocked, whereas the WCEQ section is nearly locked (Fig. 4d).

Our results also imply that the aftershock gap between the WCEQ and the LSEQ (red ellipse in Fig. 1b) is unlikely to be a seismic asperity as this section appears to play little role in the stress redistribution between the Wenchuan and the Lushan segments. We expect the stress redistribution would have been largely shielded if a strong asperity were present between the two seismic segments. A weak gap section is also consistent with recent seismic tomography results[32], which indicate that the gap region is underlaid by a lower seismic velocity compared to that of the surrounding regions.

Online content

Any methods, additional references, Nature Research reporting summaries, source data, statements of data availability, and associated accession codes are available at https://doi.org/10.1038/s41561-019-0347-1.

Received: 21 March 2018; Accepted: 13 March 2019;
Published online: 15 April 2019

References

1. Niu, F., Silver, P. G., Nadeau, R. M. & McEvilly, T. V. Migration of seismic scatterers associated with the 1993 Parkfield aseismic transient event. *Nature* **426**, 544–548 (2003).
2. Schaff, D. P. & Beroza, G. C. Coseismic and postseismic velocity changes measured by repeating earthquakes. *J. Geophys. Res.* **109**, B10302 (2004).
3. Peng, Z. & Ben-Zion, Y. Temporal changes of shallow seismic velocity around the Karadere–Duzce branch of the North Anatolian fault and strong ground motion. *Pure Appl. Geophys.* **163**, 567–599 (2006).
4. Niu, F., Silver, P. G., Daley, T. M., Cheng, X. & Majer, E. L. Preseismic velocity changes observed from active source monitoring at the Parkfield SAFOD drill site. *Nature* **454**, 204–208 (2008).
5. Brenguier, F. et al. Postseismic relaxation along the San Andreas fault at Parkfield from continuous seismological observations. *Science* **321**, 1478–1481 (2008).
6. Wu, C. Q., Peng, Z. G. & Ben-Zion, Y. Non-linearity and temporal changes of fault zone site response associated with strong ground motion. *Geophys. J. Int.* **176**, 265–278 (2009).
7. Bonilla, L. F., Guéguen, P. & Ben-Zion, Y. Monitoring co-seismic temporal changes of shallow material during strong ground motion with interferometry and autocorrelation. *Bull. Seism. Soc. Am.* **109**, 187–198 (2019).
8. Cheng, X., Niu, F. & Wang, B. S. Coseismic velocity change in the rupture zone of the 2008 M_w7.9 Wenchuan Earthquake observed from ambient seismic noise. *Bull. Seismol. Soc. Am.* **100**, 2539–2550 (2010).
9. Froment, B. M., Campillo, M., Chen, J. H. & Liu, Q. Y. Deformation at depth associated with the 12 May 2008 M_w7.9 Wenchuan earthquake from seismic ambient noise monitoring. *Geophys. Res. Lett.* **40**, 78–82 (2013).
10. Obermann, A. et al. Seismic noise correlations to image structural and mechanical changes associated with the M_w7.9 2008 Wenchuan earthquake. *J. Geophys. Res.* **119**, 3155–3168 (2014).
11. Lay, T. & Kanamori, H. Insights from the great 2011 Japan earthquake. *Phys. Today* **64**, 33–39 (2011).
12. Murray, J. R. & Segall, P. Spatiotemporal evolution of a transient slip event on the San Andreas fault near Parkfield, California. *J. Geophys. Res.* **110**, B09407 (2005).
13. Obara, K. Nonvolcanic deep tremor associated with subduction in southwest Japan. *Science* **296**, 1679–1681 (2002).
14. Rogers, G. & Dragert, H. Episodic tremor and slip on the Cascadia subduction zone: the chatter of silent slip. *Science* **300**, 1942–1943 (2003).
15. Nadeau, R. M. & Dolenc, D. Nonvolcanic tremors deep beneath the San Andreas fault. *Science* **307**, 389 (2005).
16. Xiong, X. et al. Coulomb stress transfer and accumulation on the Sagaing Fault, Myanmar, over the past 110 years and its implications for seismic hazard. *Geophys. Res. Lett.* **44**, 4781–4789 (2017).
17. Freed, A. M. & Lin, J. Delayed triggering of the 1999 Hector Mine earthquake by viscoelastic stress transfer. *Nature* **411**, 180–183 (2001).
18. Toda, S., Stein, R. S., Reasonberg, P. A. & Dieterich, J. H. Stress transferred by the M_w=6.5 Kobe, Japan, shock: effect on aftershocks and future earthquake probabilities. *J. Geophys. Res.* **103**, 24543–24565 (1998).
19. Stein, R. S. The role of stress transfer in earthquake occurrence. *Nature* **402**, 605–609 (1999).
20. Pollitz, F., Vergnolle, M. & Calais, E. Fault interaction and stress triggering of twentieth century earthquakes in Mongolia. *J. Geophys. Res.* **108**, 2503 (2003).

21. Parsons, T., Ji, C. & Kirby, E. Stress changes from the 2008 Wenchuan earthquake and increased hazard in the Sichuan basin. *Nature* **454**, 509–510 (2008).
22. Yamamura, K. et al. Long-term observation of in situ seismic velocity and attenuation. *J. Geophys. Res.* **108**, B2317 (2003).
23. Birch, F. The velocity of compressional waves in rocks to 10 kilobars, part 1. *J. Geophys. Res.* **65**, 1083–1102 (1960).
24. Birch, F. The velocity of compressional waves in rocks to 10 kilobars, part 2. *J. Geophys. Res.* **66**, 2199–2224 (1961).
25. Nur, A. & Simmons, G. The effect of saturation on velocity in low porosity rocks. *Earth Planet. Sci. Lett.* **7**, 183–193 (1969).
26. Yamada, M., Mori, J. & Ohmi, S. Temporal changes of subsurface velocities during strong shaking as seen from seismic interferometry. *J. Geophys. Res.* **115**, B03302 (2010).
27. Sawazaki, K., Sato, H., Nakahara, H. & Nishimura, T. Time-lapse changes of seismic velocity in the shallow ground caused by strong ground motion shock of the 2000 western Tottori earthquake, Japan, as revealed from coda deconvolution analysis. *Bull. Seismol. Soc. Am.* **99**, 352–366 (2009).
28. Nakata, N. & Snieder, R. Near-surface weakening in Japan after the 2011 Tohoku-Oki earthquake. *Geophys. Res. Letters.* **38**, L17302 (2011).
29. Sens-Schönfelder, C. & Wegler, U. Passive image interferometry and seasonal variations of seismic velocities at Merapi volcano, Indonesia. *Geophys. Res. Lett.* **33**, L21302 (2006).
30. Brenguier, F. et al. Towards forecasting volcanic eruptions using seismic noise. *Nat. Geosci.* **1**, 126–130 (2008).
31. Pei, S. P. & Chen, Y. J. Link between seismic velocity structure and the 2010 M_s7.1 Yushu earthquake, Qinghai, China: evidence from aftershock tomography. *Bull. Seismol. Soc. Am.* **102**, 445–450 (2012).
32. Pei, S. P., Zhang, H. J., Su, J. R. & Cui, Z. X. Ductile gap between the Wenchuan and Lushan earthquakes revealed from the two-dimensional Pg seismic tomography. *Sci. Rep.* **4**, 6489 (2014).
33. Ji, C. & Hayes, G. *Preliminary Result of the May 12, 2008* M_w 7.9 Eastern Sichuan, China E (USGS, 2008); https://web.archive.org/web/20080517072013/http://earthquake.usgs.gov/eqcenter/eqinthenews/2008/us2008ryan/finite_fault.php
34. Feng, G. C., Hetland, E. A., Ding, X. L., Li, Z. W. & Zhang, L. Coseismic fault slip of the 2008 M_w7.9 Wenchuan earthquake estimated from InSAR and GPS measurements. *Geophys. Res. Lett.* **37**, L01302 (2010).
35. Diao, F., Xiong, X., Wang, R., Zheng, Y. & Hsu, H. Slip model of the 2008 M_w7.9 Wenchuan (China) earthquake derived from co-seismic GPS data. *Earth Planets Space* **62**, 869–874 (2010).
36. Fu, B. et al. Surface deformation related to the 2008 Wenchuan earthquake, and mountain building of the Longmen Shan, eastern Tibetan Plateau. *J. Asian Earth Sci.* **40**, 805–824 (2011).
37. Xu, X. W. et al. Coseismic reverse- and oblique-slip surface faulting generated by the 2008 M_w7.9 Wenchuan earthquake, China. *Geology* **37**, 515–518 (2009).
38. Efron, B. & Tibshirani, R. Bootstrap methods for standard errors, confidence intervals, and other measures of statistical accuracy. *Stat Sci.* **1**, 54–77 (1986).
39. Yang, C., Li, G., Niu, F. & Ben-Zion, Y. Significant effects of shallow seismic and stress properties on phase velocities of Rayleigh waves up to 20 s. *Pure Appl. Geophys.* **176**, 1255–1267 (2019).
40. Vidale, J. E. & Li, Y. G. Damage to the shallow Landers fault from the nearby Hector Mine earthquake. *Nature* **421**, 524–526 (2003).
41. Taira, T., Silver, P. G., Niu, F. & Nadeau, R. M. Remote triggering of fault-strength changes on the San Andreas Fault at Parkfield. *Nature* **461**, 636–639 (2009).
42. Freed, A. M. Earthquake triggering by static, dynamic and postseismic stress transfer. *Annu. Rev. Earth Planet. Sci.* **33**, 335–367 (2005).
43. Qiu, J. et al. Comparative analysis of in-situ stress state in the southwestern segment of the Longmenshan fault zone before and after the Lushan earthquake. *Acta Geol Sin.* **91**, 969–978 (2017).

Acknowledgements

We thank the EASP and the Center of the China Earthquake Networks for providing the seismic data in this study. This work was supported by the Strategic Priority Research Program of Chinese Academy of Sciences (XDA20070302), the National Key R&D Program of China (2016YFC0600303) and the National Natural Science Foundation of China (41674090, 41490610).

Author contributions

Q.S., Y.L., X.X., J.S. and Z.S. were responsible for collecting the travel time data; S.P. developed the new 4D tomography method and conducted the inversions; S.P., F.N. and Y.B.-Z. contributed to the interpretations and writing; F.N. took the lead on writing the manuscript.

Competing interests

The authors declare no competing interests.

Additional information

Supplementary information is available for this paper at https://doi.org/10.1038/s41561-019-0347-1.

Reprints and permissions information is available at www.nature.com/reprints.

Correspondence and requests for materials should be addressed to F.N.

Publisher's note: Springer Nature remains neutral with regard to jurisdictional claims in published maps and institutional affiliations.

Methods

As all the earthquakes occurred in the upper-to-middle crust and were recorded at distance less than 2°, we first assumed that the Pg waves propagate through a straight line that connects the source and the receiver[31,32]. We further projected the hypocentres to the epicentres and approximated the ray paths with horizontal lines from epicentres to the receivers. The difference in the true ray path and horizontal ray path is expected to be small when the source depth (h) is much smaller than the epicentral distance (Δ), which is generally true for most of the ray paths used in our inversion. We further made correction to the observed travel time due to this difference:

$$t_0^c = t_0 - \{(h^2 + \Delta^2)^{1/2} - \Delta\} s_o \quad (1)$$

Here t_0 and t_0^c are the original and corrected Pg travel time, and s_o is the average slowness computed from the linear regression described above. We further introduced a station (a_r) and a source (b_e) term to the corrected observed Pg travel time:

$$t_0^c = t_{tt} + a_r + b_e \quad (2)$$

where t_{tt} is the true travel time along the horizontal ray path. The station correction term is expected to absorb site effects, which include instrument uncertainties and anomalies related to the very shallow velocity structure around the station[44]. The event correction term mainly takes care of the errors in focal depth and origin time of an earthquake.

We further discretized the upper crust of the study area into small 2D cells, each cell with a slowness perturbation δs_k with respect to the average slowness computed from slope of the Pg travel times. Then the travel time residual for the Pg ray path between event j and station i can be written as:

$$\delta t_{ij} = t_0^c - t_c = a_i + b_j + \sum_k d_{ijk} \delta s_k \quad (3)$$

where d_{ijk} is the segment length of the Pg ray within the cell k and t_c is the computed travel time. Based on the Pg travel time data, we set up two sets of linear equations[3] for two different periods. For the second period, we write the slowness perturbation in the second period as the summation of the background perturbation (that is, the slowness perturbation in the first period, δs_k) and a temporal change term, Δs_k. More specifically we can express the two sets of equations that share some common unknowns:

$$\mathbf{A}\begin{bmatrix}\delta\mathbf{s}\\ \mathbf{a_1}\\ \mathbf{b_1}\end{bmatrix} = A\mathbf{x_1} = \delta t_1 B\begin{bmatrix}\delta\mathbf{s}\\ \Delta\mathbf{s}\\ \mathbf{a_2}\\ \mathbf{b_2}\end{bmatrix} = B\mathbf{x_2} = \delta t_2 \quad (4)$$

Note here the station terms of the two periods (a_1 and a_2) are solved jointly if the stations used in the two periods are exactly the same. The two sets of the equations in equation (74) are solved jointly with a spatial smoothing and temporal damping:

$$\lambda_1 \mathbf{L}\delta s = 0 \lambda_2 \mathbf{\Delta} s = 0 \quad (5)$$

Here, $\boldsymbol{L}$ is the Laplacian operator and λ_1 and λ_2 are the smoothing and damping parameters, respectively. We then solve the equations (74) and (75) using a LSQR algorithm[45] with a spatial preconditioning to find the least-squares solution that minimizes the following function:

$$\|\mathbf{A x_1} - \mathbf{\delta t_1}\|^2 + \|\mathbf{B x_2} - \mathbf{\delta t_2}\|^2 + \lambda_1^2 \|\mathbf{L}\delta s\|^2 + \lambda_2^2 \|\mathbf{\Delta} s\|^2 \quad (6)$$

As shown in Supplementary Figs. 5 and 6, the chequerboard tests indicate that the lateral resolution of our Pg data set is ~0.25° × 0.25°. To keep the 3D blocks at roughly the same size in the depth and lateral directions, we decided to treat the ~20 km upper crust as a single layer and employed a 2D tomographic inversion in mapping the subsurface velocity changes.

Data availability

The travel time data are provided by the Sichuan Earthquake Administration and the China Earthquake Data Centre and are available at http://data.earthquake.cn/.

Code availability

The codes used to generate individual results are available through the contact information from the original publications. Requests for further materials should be directed to S.P. (peisp@itpcas.ac.cn).

References

44. Pujol, J. Comments on the joint determination of hypocenters and station corrections. *Bull. Seismol. Soc. Am.* **78**, 1179–1189 (1988).
45. Paige, C. C. & Saunders, M. A. LSQR: an algorithm for sparse linear equations and sparse least squares. *ACM Trans. Math. Software* **8**, 43–71 (1982).